

Supporting Information

Porous Organic Polymer Derived N-doped Porous Carbon Nanoparticles for Efficient Oxygen Reduction Electrocatalysis and Supercapacitors

Mei Yang ^{a,b,*}, Xuan Long ^a, Huaming Li ^a, Hongbiao Chen ^a, Pingle Liu ^{c*}

^a College of Chemistry, Xiangtan University, Xiangtan 411105, Hunan Province, P. R. China

^b Key Laboratory of Polymeric Materials & Application Technology of Hunan Province, Key Laboratory of Advanced Functional Polymeric Materials of College of Hunan Province, and Key Lab of Environment-Friendly Chemistry and Application in Ministry of Education, Xiangtan University, Xiangtan 411105, Hunan Province, P. R. China

^c College of Chemical Engineering, Xiangtan University, Xiangtan 411105, Hunan Province, P. R. China

*Corresponding author: Tel.: +86 731 58298005; Fax: +86 731 58293549.

E-mail address: liupingle@xtu.edu.cn (P. Liu) yangmei@xtu.edu.cn (M. Yang)

Total number of pages: 17

Total number of tables: 5

Table S1: Textural and electrochemical properties for TPOP-850, TPOP-900, and TPOP-950.

Table S2: C, N, O, and H contents evaluated from elemental analysis.

Table S3: C, N, O contents of TPOP-850, TPOP-900, and TPOP-950 evaluated from XPS.

Table S4: Summary of the optimal pyrolysis temperature, BET SSA, N content and the active N (graphitic-N + pyridinic-N) content of various metal-free ORR electrocatalysts and /or supercapacitor electrode materials derived from porous organic polymers.

Table S5: Summary of the electrochemical performances of various metal-free ORR electrocatalysts and /or supercapacitor electrode materials derived from porous organic polymers.

Total number of schemes: 2

Scheme S1: Schematic representation of the synthesis of DPT.

Scheme S2: Schematic representation of the synthesis of TPOP.

Total number of figures: 9

Figure S1: ¹H NMR spectrum of DPT in CDCl₃.

Figure S2: MS spectrum of DPT.

Figure S3: FT-IR spectrum of the TPOP.

Figure S4: TGA curve of TPOT in nitrogen atmosphere at a heating rate of 10 °C min⁻¹.

Figure S5: The XPS survey spectra (a) and high-resolution N 1s (b) spectra of TPOP-850. The XPS survey spectra (c) and high-resolution N 1s (d) spectra of TPOP-950.

Figure S6: RDE voltammograms of TPOP-850, TPOP-900, and TPOP-950 in O₂-saturated 0.1 M KOH with a rotation speed of 1600 rpm (a). CV curves tested at a 5 mV s⁻¹ (b), and GC curves tested at a current density of 0.5 A g⁻¹ (c). The correlation of specific capacitances with current densities (d).

Figure S7: LSV curves of TPOP-900 with different counter electrode (a). LSV curves of TPOP-900 after cycling durability test with different counter electrode (b). Both were tested in O₂-saturated 0.1 M KOH solution at 1600 rpm.

Figure S8: CV curves tested at a 5 mV s⁻¹ (a), GC curves tested at a current density of 0.5 A g⁻¹ (b), the correlation of specific capacitances with current densities (c), and Nyquist plot (d) of YP-50F and TPOP-900.

Figure S9: Cycling performance of YP-50F and TPOP-900.

S1. Materials

Pyridine, glacial acetic acid, nitric acid, Cyanuric chloride, 4-Cyanopyridine, hydrazine monohydrate, toluene, acetone, hydrochloric acid (HCl), potassium hydroxide (KOH), and ethanol were purchased from Shanghai Aladdin Industrial Co. (China).

S2. Instruments

¹H NMR spectra was recorded with a 400 MHz Bruker AV-400 NMR spectrometer and chemical shifts were recorded in ppm units with TMS as the internal standard. Mass spectra were collected by a Microflex LRF MALDI-TOF mass spectrometer (Bruker Daltonics, USA).

Thermogravimetric analysis (TGA) was carried out on a STA 449C instrument with a heating rate of 10 °C min⁻¹ under a nitrogen flow rate of 100 mL min⁻¹. Fourier transform infrared (FT-IR) spectra of samples prepared as KBr pellets were recorded on a Nicolet 6700 spectrophotometer.

Elemental analysis (EA) was conducted with a Perkin-Elmer CHN 2400 analyzer. The textural properties were characterized by N₂ sorption measurements at 77.3 K (Micromeritics TriStar II 3020). The specific surface area was obtained by Brunauer-Emmett-Teller (BET) method. The pore size distribution (PSD) was calculated from the adsorption branches of the isotherms using the DFT model. Scanning electron microscopy (SEM) images were recorded using S-4800 (JEOL) operated at an acceleration voltage of 10 kV. The transmission electron microscopy (TEM) images were recorded on a JEOL JEM-1011 transmission electron microscope (Japan) operating at 200 kV. The X-ray photoelectron spectroscopy (XPS) was performed on a K-Alpha 1063

photoelectron spectrometer (Thermo Fisher Scientific, England) with Al-K α X-ray radiation as the X-ray source for excitation. Raman spectra were recorded using a Renishaw via Raman spectrometer at 25 °C. The spectral were recorded over the range of 200–3200 cm⁻¹ using the 532 nm emission of an Ar ion laser source, and the resolution was 1 cm⁻¹. Powder X-ray diffraction (XRD) was performed on a Rigaku D/Max 2500PC diffractometer.

S3. ORR

ORR tests were performed on a CHI760D electrochemical analyzer (Chenhua Instruments, Shanghai, China). Glassy carbon electrode (GC) with geometric area of 0.196 cm² was used as a substrate material. The ORR activity was then evaluated by cyclic voltammetry (CV) and linear sweep voltammetry (LSV) techniques on rotating disk electrode (RDE, AFE5T050GC, Pine Research Instrumentation, USA) in O₂-saturated 0.1 M KOH solution. Rotating ring-disk electrode (RRDE, AFE7R9GCPT, Pine Research Instrumentation, USA) measurements were carried out to determine the four-electron selectivity. The disk electrode was scanned at a rate of 10 mV s⁻¹, and the ring electrode potential was set to 0.5 V (vs. Ag/AgCl) in 0.1 M KOH. Methanol tolerant, CO poisoning and durability testing were conducted by chronoamperometric technique at the bias potential of -0.3 V (vs. Ag/AgCl) in O₂-saturated 0.1 M KOH electrolyte at 1600 rpm. The Koutecky-Levich plots were obtained by linear fitting of the reciprocal rotating speed versus reciprocal current density collected at different potentials. The overall electron transfer numbers (n) per oxygen molecule involved in a typical ORR process were calculated from the slopes of Koutecky-Levich plots using the following equation:

$$1/J = 1/J_k + 1/(B\omega^{1/2}) \quad (\text{Equation S1})$$

where J is the measured current density, J_k is the kinetic current density, ω is the electrode rotating speed in rpm, and B , the reciprocal of the slope, which was determined from the slope of Koutecky-Levich plots based on Levich equation as followed:

$$B = 0.2nF\nu^{-1/6}C_{O_2}D_{O_2}^{2/3} \quad (\text{Equation S2})$$

where n is the number of electrons transferred per oxygen molecule, F is the Faraday constant (96485 C mol⁻¹). The diffusion coefficient of oxygen D_{O_2} in 0.1 M KOH is 1.9×10^{-5} cm² s⁻¹, ν is the kinetic viscosity (0.01 cm² s⁻¹), and the concentration of oxygen C_{O_2} is 1.2×10^{-3} mol L⁻¹. The constant 0.2 is adopted when the rotating speed is in rpm.

The RRDE measurements were also conducted to determine peroxide species formed and the electron transfer number (n). The disk electrode was scanned at a rate of 10 mV s⁻¹ and the ring electrode potential in the RRDE system was set to 0.5 V (vs. Ag/AgCl). The yield of peroxide species (%HO₂⁻ in alkaline media, %H₂O₂ in acidic media) and the number of electron transfer (n) were calculated by the followed equations:

$$\%HO_2^- \text{ (or \%H}_2O_2\text{)} = 200 \times \frac{i_r / N}{i_r / N + i_d} \quad (\text{Equation S3})$$

$$n = 4 \times \frac{i_d}{i_r / N + i_d} \quad (\text{Equation S4})$$

where i_d and i_r are the disk and ring currents, respectively. N is the ring current collection efficiency, which was determined to be 37 % by the reduction of 10 mM K₃[Fe(CN)₆] in 0.1 M KNO₃.

S4. Supercapacitors

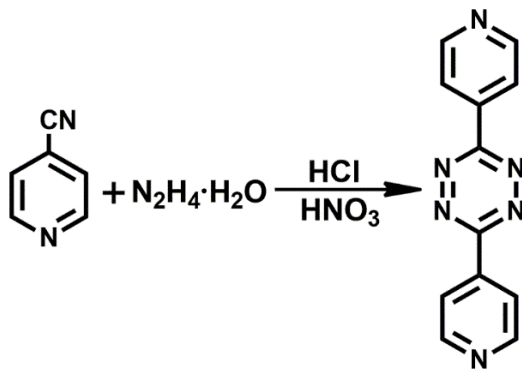
The specific capacitance (C_g) for three electrode test was calculated from the discharge curve according to the following equation:

$$C_g = I/(mdV/dt) \quad (\text{Equation S5})$$

where I (A) is the constant current, m is the mass of the active material and dV/dt is calculated from the slope obtained by fitting a straight line to the discharge curve from the end of the voltage drop to the end of the discharge process.

S5. Synthesis of DPT monomer

DPT was synthesized according to the procedure reported previously by Hupp group.¹ 4-Cyanopyridine (5.5 g, 52.8 mmol), hydrazine monohydrate (25 mL), concentrated HCl (5 mL), and deionized water (5 mL) were refluxed together for 2 h. The reaction was allowed to cool to room temperature. The precipitate (orange solid) was filtered and added to 200 mL of glacial acetic acid with stirring. A 35 mL of 30% HNO_3 was added dropwise to the brown solution. The pink solid was collected by filtrations and recrystallized from pyridine to yield a purple solid, yield: 56%.



Scheme S1. Schematic representation of the synthesis of DPT.

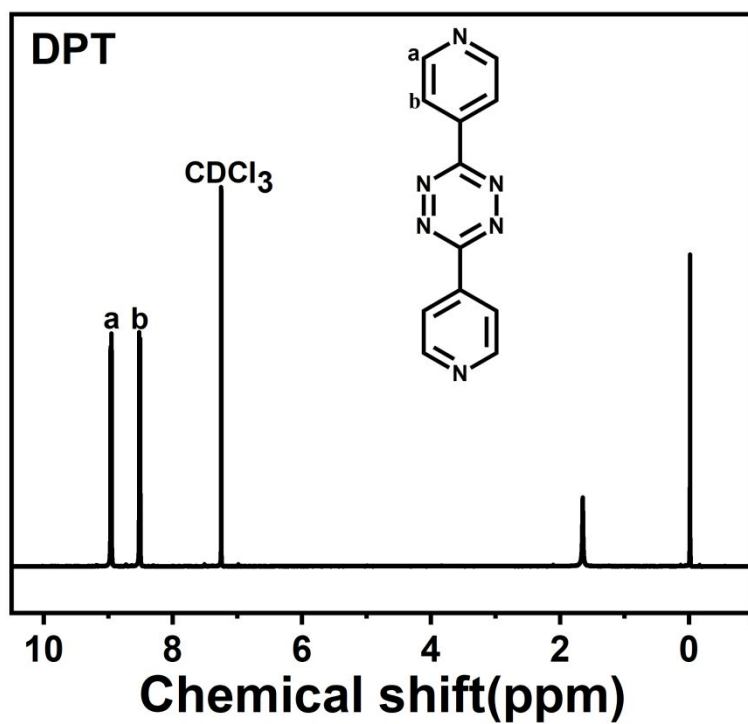


Figure S1. ¹H NMR spectrum of DPT in CDCl₃.

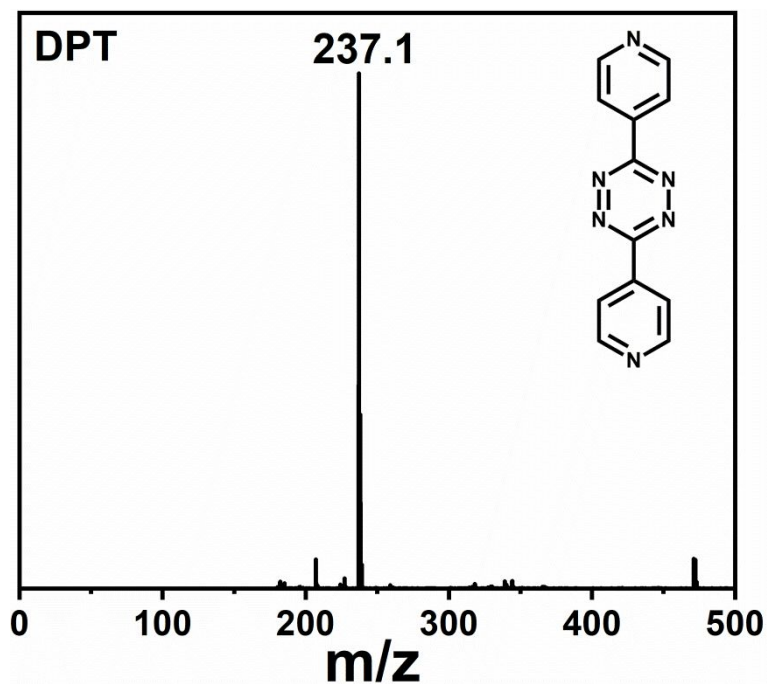
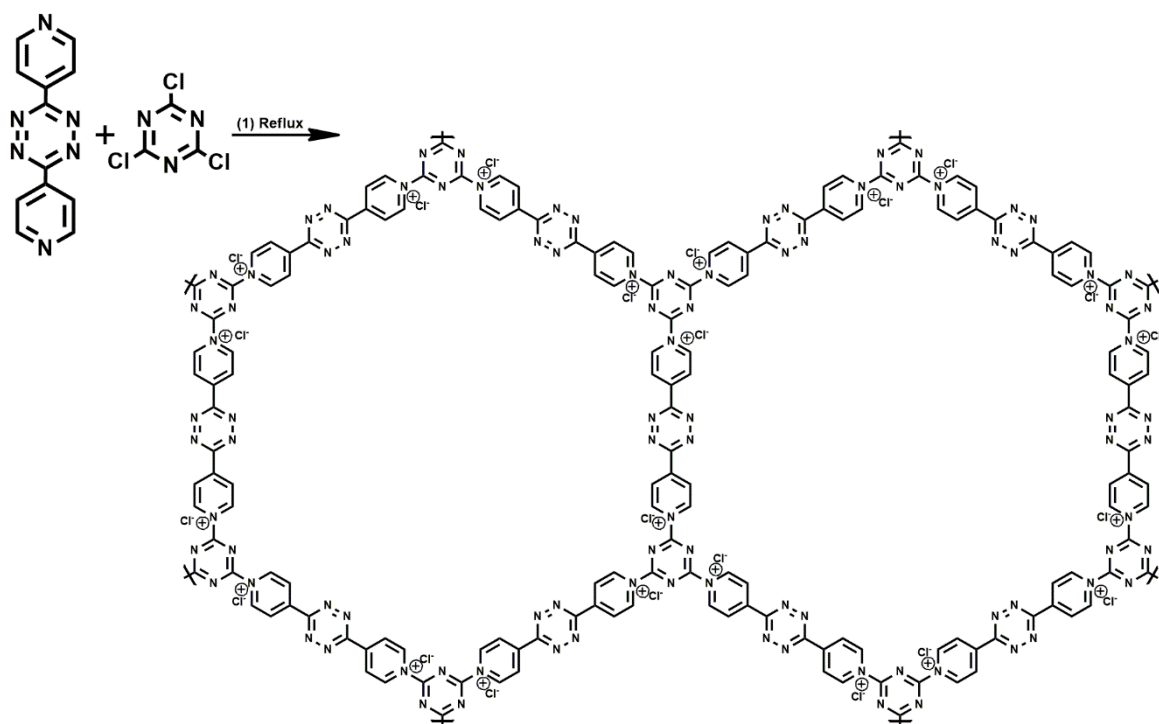


Figure S2. MS spectrum of DPT.



Scheme S2. Schematic representation of the synthesis of TPOP.

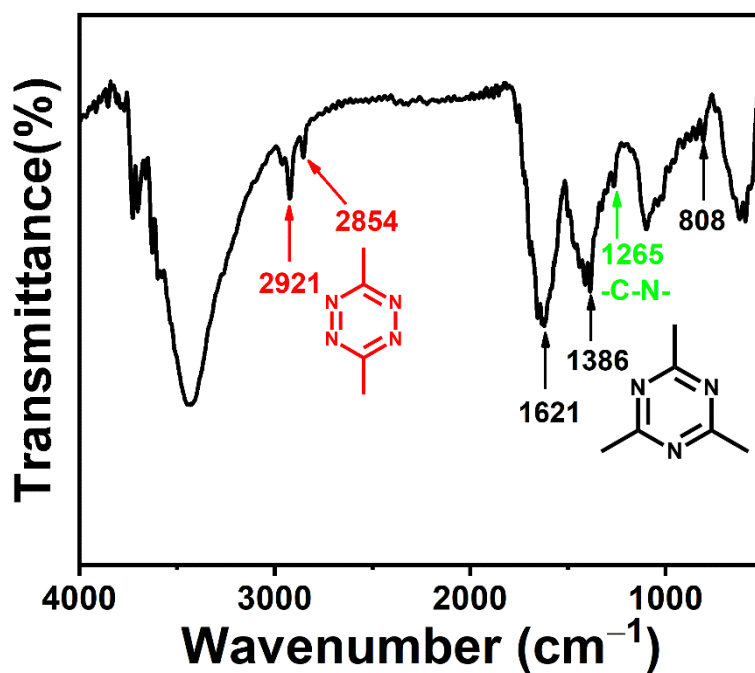


Figure S3. FT-IR spectrum of the TPOP. The peak at 1265 cm^{-1} corresponds to the stretching vibration of C-N, while the peaks at 1621, 1386, and 808 cm^{-1} correspond to the typical stretching modes of triazine heterocycle. The peak at 2921, 2854 cm^{-1} correspond to the typical stretching modes of tetrazine heterocycle.

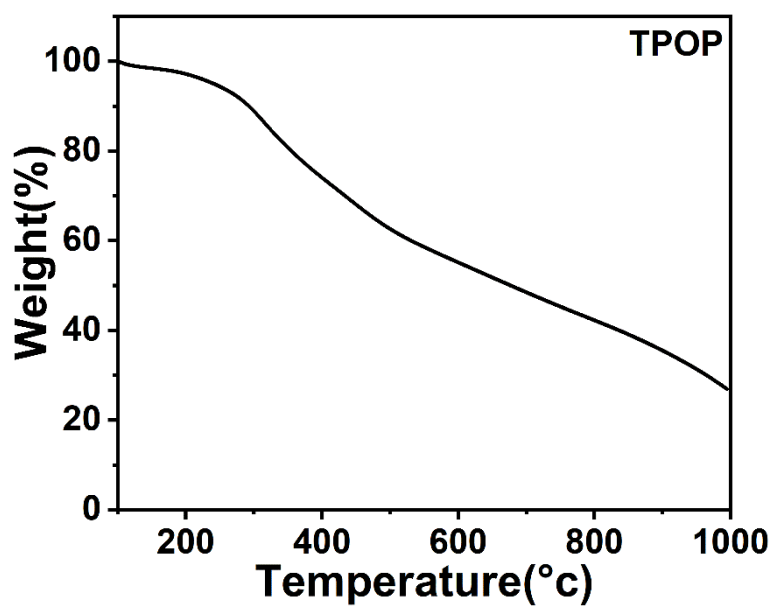


Figure S4. TGA curve of TPOP in nitrogen atmosphere at a heating rate of 10 °C min⁻¹.

Table S1. Textural and electrochemical properties for TPOP-850, TPOP-900, and TPOP-950.

Samples	BET SSA (m ² g ⁻¹)			Pore volume (cm ³ g ⁻¹)			E_o^a (V)	J_L^b (mA cm ⁻²)
	Total	Micro	External	Total	Micro	External		
TPOP-850	531	518	12	0.36	0.32	0.10	-0.004	-5.00
TPOP-900	574	552	22	0.46	0.41	0.19	0.011	-5.20
TPOP-950	740	716	23	0.50	0.45	0.16	-0.007	-4.95

^a ORR onset potential in O₂ saturated 0.1 M KOH solution with the rotation speed of 1600 rpm.

^b Limiting current density in O₂ saturated 0.1 M KOH solution at -1.0 V (vs. Ag/AgCl).

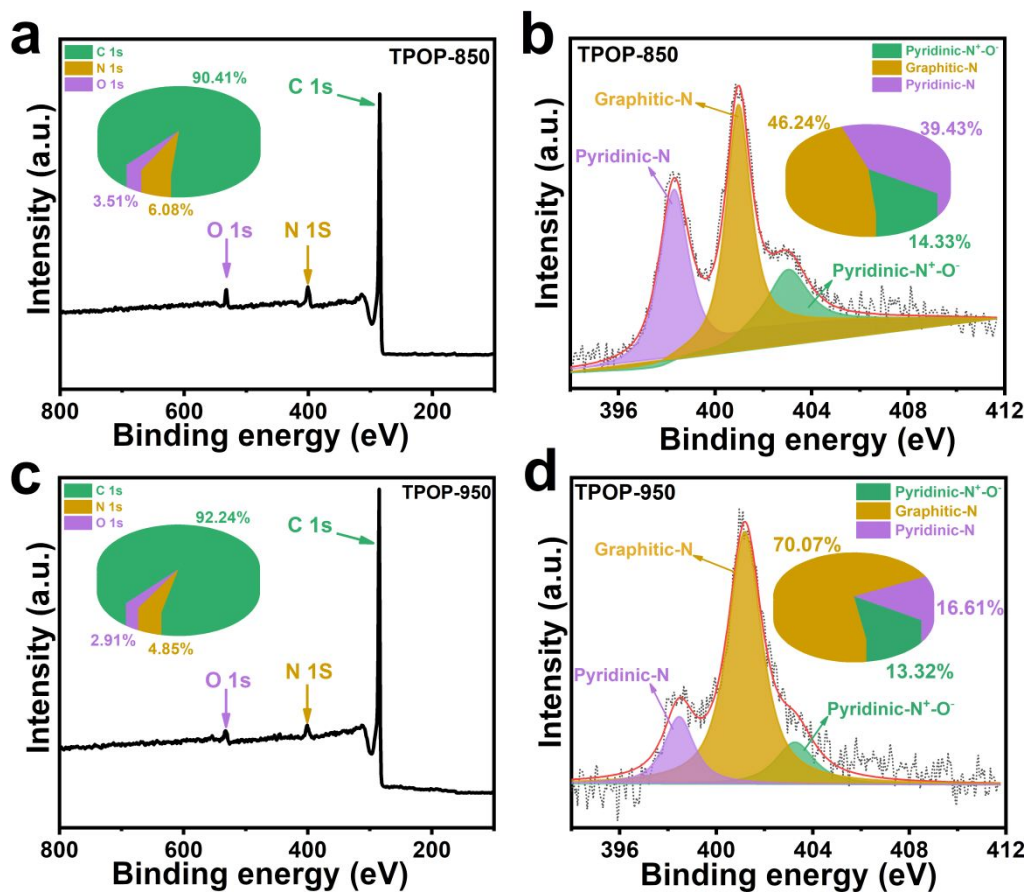


Figure S5. The XPS survey spectra (a) and high-resolution N 1s (b) spectra of TPOP-850. The XPS survey spectra (c) and high-resolution N 1s (d) spectra of TPOP-950.

Table S2. C, N, O, and H contents evaluated from elemental analysis.

Samples	Elemental Analysis ^a			
	C (wt.%)	N (wt.%)	O ^b (wt.%)	H (wt.%)
TPOP-850	84.47	9.75	3.28	2.50
TPOP-900	87.65	7.51	2.97	1.87
TPOP-950	89.56	5.48	2.80	2.16

^a Elemental analysis was carried out on the CHNS elemental analyzer (Vario EL, Elementar, Germany).

^b The content of oxygen was calculated by the difference to 100%, neglecting the ash content.

Table S3. C, N, O contents of TPOP-850, TPOP-900, and TPOP-950 evaluated from XPS.

Samples	XPS					
	Elemental content (at.%)			N configuration ^a (%)		
	C	N	O	N-P	N-Q	N-X
TPOP-850	90.41	6.08	3.51	39.43	46.24	14.33
TPOP-900	91.17	5.63	3.20	27.99	67.52	4.49
TPOP-950	92.24	4.85	2.91	16.61	70.07	13.32

^a Pyridinic-N (N-P), Graphitic-N (N-Q), Pyridinic-N⁺-O⁻ (N-X).

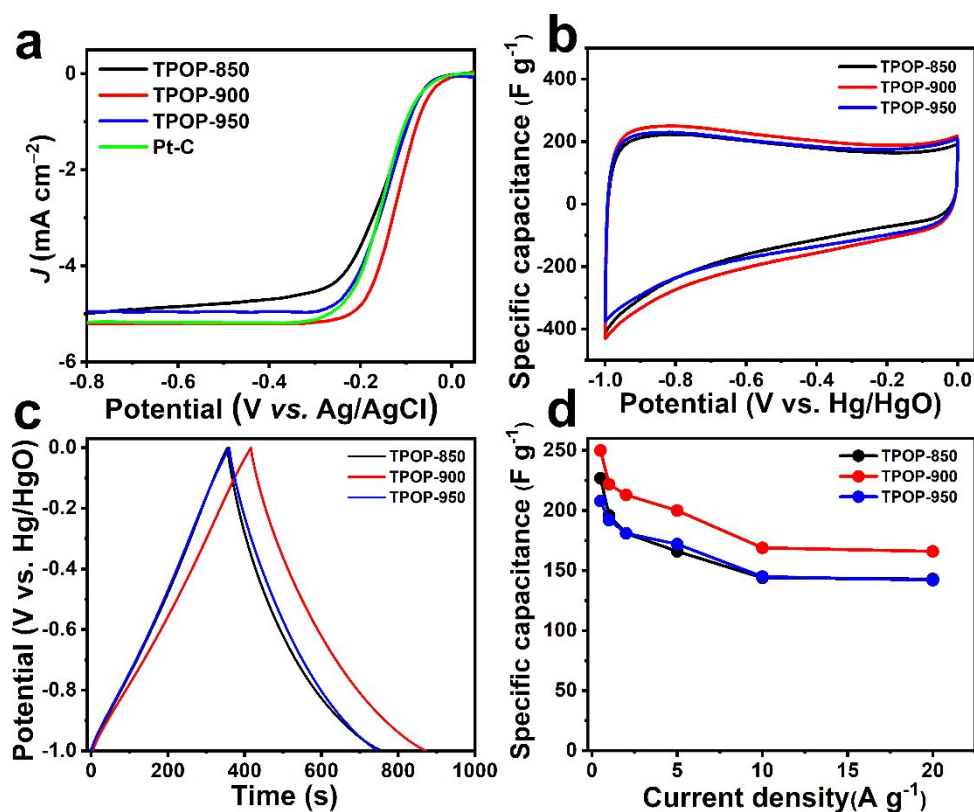


Figure S6. RDE voltammograms of TPOP-850, TPOP-900, and TPOP-950 in O_2 -saturated 0.1 M KOH with a rotation speed of 1600 rpm (a). CV curves tested at a 5 mV s $^{-1}$ (b), and GC curves tested at a current density of 0.5 A g $^{-1}$ (c). The correlation of specific capacitances with current densities (d).

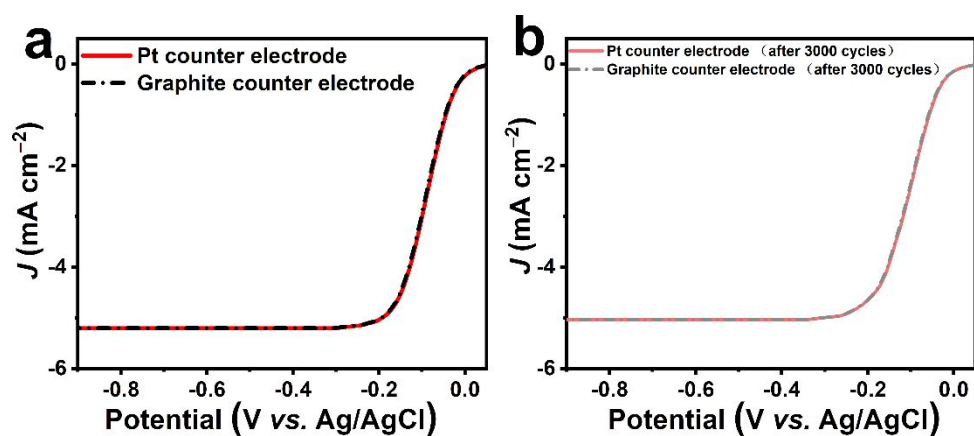


Figure S7. LSV curves of TPOP-900 with different counter electrode (a). LSV curves of TPOP-900 after cycling durability test with different counter electrode (b). Both were tested in O_2 -saturated 0.1 M KOH solution at 1600 rpm.

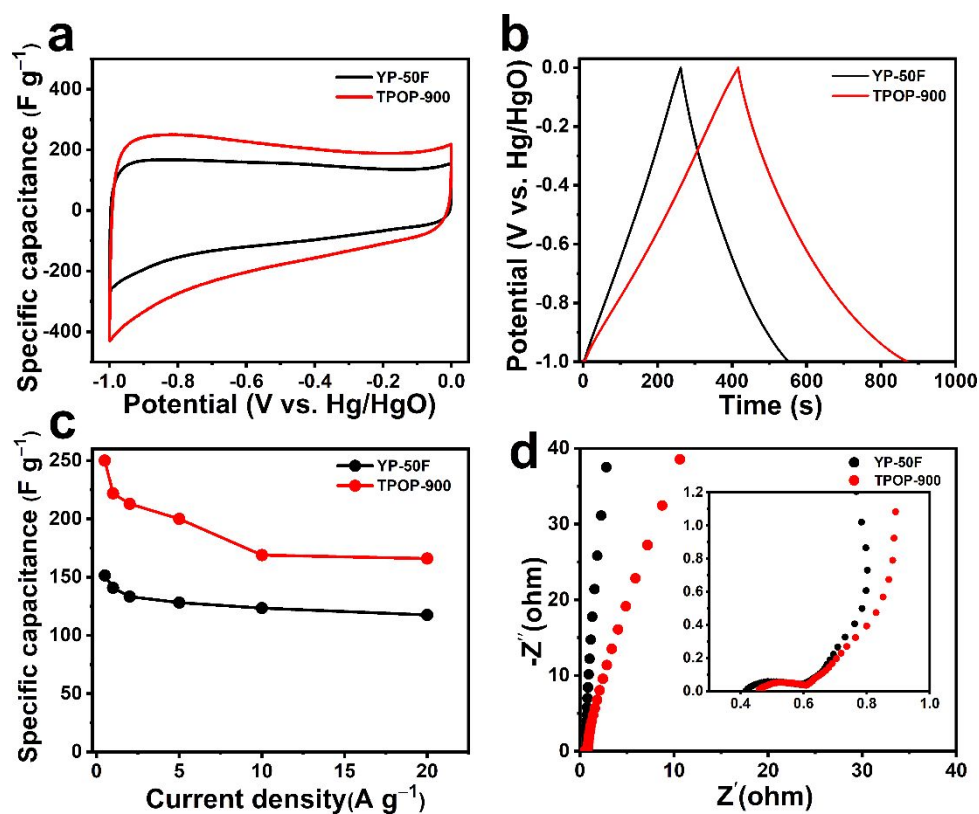


Figure S8. CV curves tested at a 5 mV s^{-1} (a), GC curves tested at a current density of 0.5 A g^{-1} (b), the correlation of specific capacitances with current densities (c), and Nyquist plot (d) of YP-50F and TPOP-900.

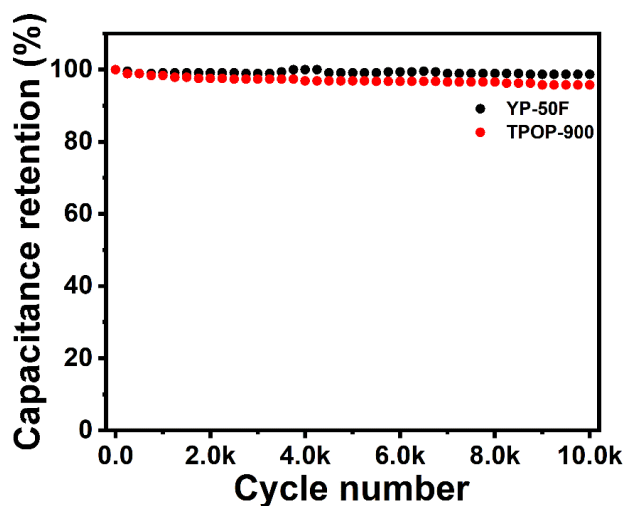


Figure S9. Cycling performance of YP-50F and TPOP-900.

Table S4. Summary of the optimal pyrolysis temperature, BET SSA, N content and the active N (graphitic-N + pyridinic-N) content of various metal-free ORR electrocatalysts and /or supercapacitor electrode materials derived from porous organic polymers.

Precursors	Pyrolysis temperature (°C)	SSA BET (m ² g ⁻¹)	N content (at.%)	Graphitic-N +pyridinic-N (%)	Ref.
Poly(triazine-thiophene-benzene)	800	700	1.15	~89.0	[2]
Poly(trianiline-dihydroxyterephthalaldehyde)	1000	1160	1.86	97.67	[3]
Poly(o-methylaniline)	900	727.1	2.00	60.0	[4]
Poly(triformylbenzene-phenylenediamine)	800	525	4.73	~85.0	[5]
Polyisocyanurate	1000	889	1.70	~45.0	[6]
Polyaniline-polypyrrole	900	645.3	3.50	91.0	[7]
Poly-terephthalonitrile	600	2570	4.73	73.01	[8]
Poly(bromo-phenyl)-triazine	950	569	3.31	~88.0	[9]
(Phytic acid)-doped polypyrrole	900	305	3.56	83.44	[10]
Triazine-based polypyrrole	900	779	3.02	65.03	[11]
Poly-melamine (amino trimethylene phosphonic acid)	900	743	3.48	54.38	[12]
Tetrazine-containing porous organic polymer	900	574	5.63	95.51	This work

Table S5. Summary of the electrochemical performances of various metal-free ORR electrocatalysts and /or supercapacitor electrode materials derived from porous organic polymers.

Precursors	Cycling performance (cycle number)	E_o^a (V vs Ag/AgCl)	J_L^b (mA cm ⁻²)	C_g^c (F g ⁻¹)	Ref.
Poly(triazine-thiophene-benzene)	83.0% (10000)	-0.005	4.10	151	[2]
Poly(trianiline-dihydroxyterephthalaldehyde)	/	0	7.20	/	[3]
Poly(o-methylaniline)	93.0% (3000)	0.016	4.10	182	[4]
Poly(triformylbenzene-phenylenediamine)	98.0% (1500)	/	/	211	[5]
Polyisocyanurate	/	-0.115	8.00	/	[6]
Polyaniline-polypyrrole	/	0.011	4.40	/	[7]
Poly-terephthalonitrile	/	-0.105	4.90	/	[8]
Poly(bromo-phenyl)-triazine	/	0	5.00	180	[9]
(Phytic acid)-doped polypyrrole	/	0	5.10	/	[10]
Triazine-based polypyrrole	/	0.007	5.05	/	[11]
Poly-melamine (amino trimethylene phosphonic acid)	/	-0.045	5.50	/	[12]
Tetrazine-containing porous organic polymer	95.7% (10000)	0.011	5.20	222	This work

^a ORR onset potential in O₂ saturated 0.1 M KOH solution with the rotation speed of 1600 rpm.

^b Limiting current density in O₂ saturated 0.1 M KOH solution at -1.0 V (vs. Ag/AgCl).

^c The specific capacitances at 1 A g⁻¹ in 6 M KOH electrolyte.

References

- [1] Farha, O. K.; Malliakas, C. D.; Kanatzidis, M. G.; Hupp, J. T.; Control over catenation in metal-organic frameworks via rational design of the organic building block. *J. Am. Chem. Soc.* **2009**, 132 (3), 950–952, DOI 10.1021/ja909519e.
- [2] Bhosale, M. E.; Illathvalappil, R.; Kurungot, S.; Krishnamoorthy, K.; Conjugated porous polymers as precursors for electrocatalysts and storage electrode materials. *Chem. Commun.* **2016**, 52 (2), 316–318, DOI 10.1039/C5CC08148C.
- [3] Xu, Q.; Tang, Y.; Zhang, X.; Oshima, Y.; Chen, Q.; Jiang, D.; Template conversion of covalent organic frameworks into 2D conducting nanocarbons for catalyzing oxygen reduction reaction. *Adv. Mater.* **2018**, 30 (15), 1706330, DOI 10.1002/adma.201706330.
- [4] He, Y.; Han, X.; Du, Y.; Song, B.; Xu, P.; Zhang, B.; Bifunctional nitrogen-doped microporous carbon microspheres derived from poly (o-methylaniline) for oxygen reduction and supercapacitors. *ACS Appl. Mater. Interfaces* **2016**, 8 (6), 3601–3608, DOI 10.1021/acsami.5b07865.
- [5] Liu, X.; Zhou, L.; Zhao, Y.; Bian, L.; Feng, X.; Pu, Q.; Hollow, spherical nitrogen-rich porous carbon shells obtained from a porous organic framework for the supercapacitor. *ACS Appl. Mater. Interfaces* **2013**, 5 (20), 10280–10287, DOI 10.1021/am403175q.
- [6] Chandrasekaran, N.; Selvakumar, K.; PremKumar, V.; Muthusamy, S.; Senthil Kumar, S. M.; Thangamuthu, R.; Dual heteroatom-doped carbon monoliths derived from catalyst-free preparation of porous polyisocyanurate for oxygen reduction reaction. *ACS Sustainable Chem. Eng.* **2018**, 6 (7), 9094–9103, DOI 10.1021/acssuschemeng.8b01440.
- [7] He, J.; He, Y.; Fan, Y.; Zhang, B.; Du, Y.; Wang, J.; Xu, P.; Conjugated polymer-mediated synthesis of nitrogen-doped carbon nanoribbons for oxygen reduction reaction. *Carbon*, **2017**, 124,

630–636, DOI 10.1016/j.carbon.2017.08.081.

[8] Zhang, L. S.; Liu, R.; Ning, J.; Zhang, G.; Zhi, L.; Bottom-up construction of triazine-based frameworks as metal-free electrocatalysts for oxygen reduction reaction. *Adv. Mater.* **2015**, 27 (20), 3190–3195, DOI 10.1002/adma.201500863.

[9] Xiang, Z.; Cao, D.; Huang, L.; Shui, J.; Wang, M.; Dai, L.; Nitrogen-doped holey graphitic carbon from 2D covalent organic polymers for oxygen reduction. *Adv. Mater.* **2014**, 26 (20), 3315–3395, DOI 10.1002/adma.201306328.

[10] Zhang, Z.; Sun, J.; Dou, M.; Ji, J.; Wang, F.; Nitrogen and phosphorus codoped mesoporous carbon derived from polypyrrole as superior metal-free electrocatalyst toward the oxygen reduction reaction. *ACS Appl. Mater. Interfaces* **2017**, 9 (19), 16236–16242, DOI 10.1021/acsami.7b03375.

[11] Yang, M.; Liu, Y.; Chen, H.; Yang, D.; Li, H.; Porous N-doped carbon prepared from triazine-based polypyrrole network: a highly efficient metal-free catalyst for oxygen reduction reaction in alkaline electrolytes. *ACS Appl. Mater. Interfaces* **2016**, 8 (42), 28615–28623, DOI 10.1021/acsami.6b09811.

[12] Jiang, H.; Wang, Y.; Hao, J.; Liu, Y.; Li, W.; Li, J.; N and P co-functionalized three-dimensional porous carbon networks as efficient metal-free electrocatalysts for oxygen reduction reaction. *Carbon* **2017**, 122, 64–73, DOI 10.1016/j.carbon.2017.06.043.